INORGANIC CHEMISTRY FRONTIERS

RESEARCH ARTICLE

View Article Online
View Journal | View Issue

Cite this: *Inorg. Chem. Front.*, 2024, **11**, 5587

Halide-driven polarity tuning and optimized SHG-bandgap balance in $(C_4H_{11}N_2)ZnX_3$ (X = Cl, Br, I)†

Jin Chen, *[a,b] Huai-Yu Wu,[a] Miao-Bin Xu,[a] Ming-Chang Wang,[a] Qian-Qian Chen,[a] Bing-Xuan Li,[b] Chun-Li Hu*[b] and Ke-Zhao Du *[a,b]

In the quest for organic–inorganic metal halides (OIMHs) that harmoniously combine large second harmonic generation (SHG) efficiency with broad bandgaps, our study introduces a series of noncentrosymmetric and polar piperazine zinc halides, $(C_4H_{11}N_2)ZnX_3$ (X = Cl, Br, I). The distinct influence of halide anion size on the configuration of $ZnNX_3$ tetrahedra is uncovered, revealing a design principle for enhancing SHG activity and manipulating bandgap characteristics. Specifically, $(C_4H_{11}N_2)ZnCl_3$ is the first example of deep-ultraviolet (deep-UV) nonlinear optical (NLO) OIMHs, with UV transparency lower than 190 nm and moderate SHG effect, 0.8 times KH_2PO_4 (KDP). Meanwhile, compared with $(C_4H_{11}N_2)ZnI_3$ (2.1 times KDP, 4.52 eV), $(C_4H_{11}N_2)ZnBr_3$ boasts a widened bandgap of 5.53 eV while maintaining a striking SHG response (2.5 times KDP), representing a pinnacle in the SHG-bandgap balance among OIMHs with E_g exceeding 5.0 eV. Computational analyses underscore the critical roles of halide orbitals and $ZnNX_3$ distortions in dictating SHG efficiency, with increasing halide polarizability correlating with heightened SHG contributions. This study paves the way for a novel approach to designing short-UV NLO crystals based on OIMHs.

Received 15th June 2024,
Accepted 16th July 2024

DOI: 10.1039/d4qi01515k

rsc.li/frontiers-inorganic

Introduction

The interplay of light and matter at the nexus of laser physics and optical materials science unveils captivating phenomena exemplified by second harmonic generation (SHG).[1–7] This effect empowers nonlinear optical (NLO) crystals to generate a vast laser spectrum, spanning from far-infrared to the elusive deep-ultraviolet (deep-UV, λ < 200 nm) realm. Lasers penetrating the short or even deep-UV regions hold immense potential for ultrafast spectroscopy, high-density information storage, and precision instrument fabrication.[8–17] However, despite their alluring capabilities, commercialization of UV NLO crystals remains sluggish, dominated by established materials like KH_2PO_4 (KDP), β-BaB_2O_4 (BBO), and LiB_3O_5 (LBO). This lag stems from stringent performance requirements for efficient UV laser output. Ideal NLO crystals for this domain must exhibit NCS space groups, robust SHG coefficients (d_{ij} > KDP), wide bandgaps for transparency in the short or deep-UV region (E_g > 5.0 eV), moderate birefringence for phase matching (Δn > 0.04), and favorable crystal growth habits.[18–25]

Anionic groups play a pivotal role in designing NLO crystals. Planar π-conjugated $(BO_3)^{3-}$ and $(B_3O_6)^{3-}$ anions, recognized by anionic group theory, exhibit high anisotropy, large first-order hyperpolarizability, and wide HOMO–LUMO bandgaps – key factors for outstanding NLO properties.[26–31] Non-π-conjugated tetrahedra like $(PO_4)^{3-}$ and $(SO_4)^{2-}$, with their wider HOMO–LUMO gaps, also contribute as NLO building blocks, exemplified by commercially available KH_2PO_4.[32–35] Recent discoveries have yielded novel sulfate- and phosphate-based NLO crystals, such as $NH_4NaLi_2(SO_4)_2$ (1.1 × KDP),[36] $Ba_3P_3O_{10}Cl$ (0.5 × KDP),[37] $RbNaMgP_2O_7$ (1.5 × KDP),[38] $Li_9Na_3Rb_2(SO_4)_7$ (1.3 × KDP),[39] and $ZrF_2(SO_4)$ (3.2 × KDP).[40] However, tetrahedral groups often suffer from low anisotropy and polarizability due to their high symmetry, leading to challenges within NCS space groups and minimal birefringence (Δn < 0.01).[32–35] To address this limitation, researchers have explored disrupting the high symmetry of tetrahedra by partially substituting O atoms with other elements.[3,9,10,41] This strategy, exemplified by the enhanced birefringence of $LiSO_3F$ (0.057) compared to Li_2SO_4 (0.004), demonstrates the effectiveness of introducing distortion.[34] Additionally, S–O–Org units, where Org represents an organic group, have emerged as promising SHG functional units, leading to NLO crystals,[42–46] like $Ba(SO_3CH_3)_2$ (1.5 × KDP),[45] $Cs_2Mg(NH_2SO_3)_4{\cdot}4H_2O$ (2.3 × KDP),[42] and $SO_2(NH_2)_2$ (4 × KDP).[44]

[a]*College of Chemistry and Materials Science, Fujian Key Laboratory of Polymer Materials, Fujian Normal University, Fuzhou 350007, China.*
E-mail: cj2015@fjnu.edu.cn
[b]*State Key Laboratory of Structural Chemistry, Fujian Institute of Research on the Structure of Matter, Chinese Academy of Sciences, China*

†Electronic supplementary information (ESI) available. CCDC 2313121–2313123. For ESI and crystallographic data in CIF or other electronic format see DOI: https://doi.org/10.1039/d4qi01515k

On the other hand, it has been observed that the creation of M–X–Org (M: metal; X: halide; Org: organic group) asymmetric units can yield NLO OIMHs with a strong SHG effect, such as $(C_4H_{11}N_2)CdI_3$ (6 × KDP).[47–49] Furthermore, in comparison to SO_3F or S–O–Org units, M–X–Org units are more readily obtained at the experimental level, often through the controlled utilization of HX based on previously obtained MX_4-containing OIMHs.[47] However, the bandgap of $(C_4H_{11}N_2)CdI_3$, 4.10 eV, is insufficient for short UV NLO crystal applications.[47] Besides, in the case of $[C_6H_5(CH_2)_4NH_3]_4BiX_7{\cdot}H_2O$, the wider bandgap of the Br compound (3.52 eV) compared to the isomorphous I compound (2.29 eV) does not maintain a stronger SHG effect.[50] In fact, the SHG effect of the Br compound (0.4 × KDP) is significantly smaller than that of the I compound (1.3 × AGS), in which KDP: d_{33} = 0.39 pm V^{-1} and AGS: d_{36} = 12.6 pm V^{-1}. This reveals that the electronegativity-driven halogen substitution strategy does not ensure both a wide bandgap (E_g > 5.0 eV) and a strong SHG response (d_{ij} > KDP), thereby presenting a challenge in the exploration of high performance NLO in short UV band.[47–58]

To address this challenge, our efforts have been concentrated on the piperazine–Zn–Cl/Br/I system for several reasons. Firstly, the piperazine cation exhibits a wider HOMO–LUMO gap compared to the pyrazine cation (Fig. S1†), despite having a similar N-hybridized structure but lacking a π-conjugated configuration. Furthermore, d^{10} transition metals such as Zn^{2+}, Cd^{2+}, and Hg^{2+} only display weak d–d electron transitions, indicating good transparency in the UV regions. And, in contrast to toxic Cd^{2+} and Hg^{2+}, Zn^{2+} is an environmentally friendly cation. Secondly, the Zn^{2+} cation is a typical Soft Lewis Acid, while the N-hybridized piperazine is a Soft Lewis Base. Therefore, they readily form a Zn–N coordination bond, constructing polarizable Zn–X–PIP groups, which can serve as SHG functional units. Finally, it is noteworthy that replacing iodide with the smaller radius bromide can induce changes in both the polar axis and dipole moment.[59] Consequently, we have grounds to believe that halogen substitution may not only impact optical performance due to electronegativity differences but also potentially enhance the arrangement of SHG motifs through size effects, thereby influencing SHG performance. As a result, the size effect of halides could counterbalance the significant decrease in SHG effect resulting from variances in bandgap during halide substitution.

As a result, we have successfully synthesized three novel piperazine zinc halides, namely $(C_4H_{11}N_2)ZnX_3$ (X = Cl, Br, I). Notably, the UV cutoff edge of $(C_4H_{11}N_2)ZnCl_3$ falls below 190 nm, and it exhibits a moderate SHG effect at 0.8 times that of KDP, marking it as the first reported deep-UV NLO OIMHs. Additionally, when compared to $(C_4H_{11}N_2)ZnI_3$ (4.52 eV, 2.1 × KDP), $(C_4H_{11}N_2)ZnBr_3$ features an unprecedented balance between bandgap and SHG response, 5.53 eV and 2.5 × KDP, the largest value among all reported OIMHs with bandgap wider than 5.0 eV. This unusual relationship is primarily attributed to the ideally arranged $ZnNBr_3$, whereas $ZnNI_3$ not.

Experiments

Materials and synthesis

ZnO (>99%), La_2O_3 (>99%), Y_2O_3 (>99%), piperazine (>99%), HCl (36–38%, AR), HBr (48%), and HI (55–58 wt%) were used as purchased from Adamas-beta. For the synthesis of $(C_4H_{11}N_2)ZnCl_3$, the following starting materials were used: ZnO (162.78 mg, 2 mmol), piperazine (258.42 mg, 3 mmol), La_2O_3 (325.81 mg, 1 mmol), HCl (2 mL), and H_2O (1 mL). The mixture was placed in Teflon pouches (23 mL), sealed in an autoclave, heated at 110 °C for 72 hours, and then cooled to 30 °C at a rate of 1.67 °C h^{-1}. This procedure yielded colorless block-shaped crystals of $(C_4H_{11}N_2)ZnCl_3$ with approximately 95% yield based on Zn. For the synthesis of $(C_4H_{11}N_2)ZnBr_3$, the starting materials included ZnO (81.39 mg, 1 mmol), piperazine (129.21 mg, 1.5 mmol), HBr (0.3 mL), and H_2O (2 mL). The synthesis followed the same procedure, resulting in colorless block-shaped crystals of $(C_4H_{11}N_2)ZnBr_3$ with an approximate yield of 96% based on Zn. For the synthesis of $(C_4H_{11}N_2)ZnI_3$, the starting materials comprised ZnO (40.69 mg, 0.5 mmol), piperazine (172.28 mg, 2 mmol), Y_2O_3 (112.50 mg, 0.5 mmol), HI (1 mL), and H_2O (2 mL). The synthesis procedure was consistent with the aforementioned methods, leading to colorless block-shaped crystals of $(C_4H_{11}N_2)ZnI_3$ with an estimated yield of approximately 94% based on Zn.

Single crystal structure determination

Single-crystal X-ray diffraction data for the title compounds were collected on a Rigaku XtaLAB Synergy-DW dual-wavelength CCD diffractometer with Cu Kα radiation (λ = 1.54184 Å) at 109 K and 298 K. Data reduction was performed using CrysAlisPro, with absorption correction applied *via* the multi-scan method.[60] The structures of $(C_4H_{11}N_2)ZnCl_3$, $(C_4H_{11}N_2)ZnBr_3$, and $(C_4H_{11}N_2)ZnI_3$ were determined by direct methods and refined by full-matrix least-squares fitting on F^2 using SHELXL-2014.[61] All non-hydrogen atoms were refined with anisotropic thermal parameters. The structures were checked for missing symmetry elements using PLATON, and none were found.[62] The Flack parameters for $(C_4H_{11}N_2)ZnCl_3$, $(C_4H_{11}N_2)ZnBr_3$, and $(C_4H_{11}N_2)ZnI_3$ are 0.00(4), −0.06(9), and 0.053(14), respectively, confirming the correctness of their absolute structures. Additionally, twinning was observed in $(C_4H_{11}N_2)ZnBr_3$ and $(C_4H_{11}N_2)ZnI_3$, with twin laws of (−1.0, 0.0, 0.0, 0.0, −1.0, 0.0, 0.0, 0.0, −1.0). Crystallographic data, structural refinements, and crystal information of the title compounds are listed in Tables S1–S5.†

Powder X-ray diffraction

Powder X-ray diffraction (PXRD) patterns were recorded on a Rigaku Ultima IV diffractometer with graphite-monochromated Cu Kα radiation in the 2θ range of 10–70°, with a step size of 0.02°.

Thermal analysis

Thermogravimetric analysis (TGA) was conducted using a Rigaku TG-DTA 8121 unit under an Ar atmosphere, with a heating rate of 10 °C min^{-1} in the range of 30 to 650 °C.

Optical measurements

Ultraviolet–visible (UV-vis) spectra in the range of 200–800 nm were recorded on a PerkinElmer Lambda 750 UV-vis-NIR spectrophotometer. The reflectance spectrum was converted into an absorption spectrum using the Kubelka–Munk function.[63]

The infrared (IR) spectrum was recorded on a Thermo Fisher Nicolet 5700 FT-IR spectrometer in the form of KBr pellets in the range from 4000 to 400 cm^{-1}.

Second harmonic generation measurements

Powder SHG measurements were performed using a Q-switched Nd:YAG laser generating radiation at 1064 nm, following the method of Kurtz and Perry.[64] Crystalline $(C_4H_{11}N_2)ZnCl_3$, $(C_4H_{11}N_2)ZnBr_3$, $(C_4H_{11}N_2)ZnI_3$ samples were sieved into distinct particle-size ranges (45–53, 53–75, 75–105, 105–150, 150–210, and 210–300 μm). Sieved KH_2PO4 (KDP) samples in the same particle-size ranges were used as references.

Elemental analysis

The elemental content was measured using a Vario EL Cube elemental analyzer from Elementar Analysensysteme GmbH, Germany. The combustion temperature was 800 °C.

Energy-dispersive X-ray spectroscope

Microprobe elemental analyses and elemental distribution maps were obtained using a field-emission scanning electron microscope (Phenom LE) equipped with an energy-dispersive X-ray spectroscope (EDS, Phenom LE).

Computational method

The electronic structures were calculated using the plane-wave pseudopotential method within density functional theory (DFT) implemented in the CASTEP code.[65,66] For the exchange–correlation functional, we selected the Perdew–Burke–Ernzerhof (PBE) formulation within the generalized gradient approximation (GGA).[67] The interactions between the ionic cores and the electrons were described by norm-conserving pseudopotentials.[68] The following orbital electrons were treated as valence electrons: Cl-$3s^23p^5$, Br-$4s^24p^5$, I-$5s^25p^5$, Zn-$3p^54s^23d^{10}$, H-$1s^1$, C-$2s^22p^2$, and N-$2s^22p^3$. The basis set was determined using a cutoff energy of 750 eV. Monkhorst–Pack *k*-point sampling grids of 4 × 5 × 4, 4 × 5 × 4, and 1 × 1 × 1 were used for the numerical integration of the Brillouin zone.

The calculations of second-order nonlinear optical (NLO) susceptibilities were based on the length-gauge formalism within the independent particle approximation.[69,70] The second-order NLO susceptibility can be expressed as:

$$\chi^{L}_{abc}(-2\omega;\omega,\omega) = \chi^{inter}_{abc}(-2\omega;\omega,\omega) + \chi^{intra}_{abc}(-2\omega;\omega,\omega) + \chi^{mod}_{abc}(-2\omega;\omega,\omega)$$

where the subscript L denotes the length gauge, and χ^{mod}_{abc}, χ^{inter}_{abc}, and χ^{intra}_{abc} represent the contributions to χ_{abc} from interband processes, intraband processes, and the modulation of interband terms by intraband terms, respectively.

Results and discussion

Single crystals of $(H_{11}C_4N_2)ZnX_3$ (X = Cl, Br, I) were prepared through simple hydrothermal reactions. In designing the H_2O to HX ratio, we referred to the preparation conditions of $(C_4H_{12}N_2)ZnX_4$ (X = Cl, Br), which utilized 0 mL H_2O and 3 mL HX, as previously reported by our research group.[71] We found that only when the H_2O to HX ratio exceeds 2 does it facilitate the formation of coordination bonds between Zn^{2+} cations and halide anions. Powder XRD results indicate that the obtained samples are phase-pure (Fig. S2†). EDS analysis reveals that the Zn : X ratios in the Cl, Br, and I compounds are 1 : 2.86, 1 : 2.99, and 1 : 3.03, respectively (Fig. S3†). Elemental analysis of C, N, and H atoms was performed. For $(C_4H_{11}N_2)ZnCl_3$, the weight percentages were C 6.77%, H 1.63%, and N 4.02%. For $(C_4H_{11}N_2)ZnBr_3$, the weight percentages were C 8.30%, H 1.85%, and N 4.53%. For $(C_4H_{11}N_2)ZnI_3$, the weight percentages were C 8.30%, H 1.85%, and N 4.53%. IR spectra are provided in Fig. S4,† and the detailed assignments of the absorption peaks (Table S6†) are comparable with previously reported compounds.[47–49] These values are in good agreement with the crystal structure solutions.

Crystal structures

Three title compounds crystallize in different space groups (Table S1†), but they all exhibit the same topology (Fig. 1 and 2). They shared structure consists of a 2D $[(C_4H_{11}N_2)ZnX_3]_\infty$ neutral layer, which is comprised of 0D $(C_4H_{11}N_2)ZnX_3$ units connected by N–H···X hydrogen bonds. Within this structure, the 0D $(C_4H_{11}N_2)ZnX_3$ units are formed by the $ZnNX_3$ tetrahedra and piperazine cations *via* the bridging of Zn–N bonds.

$(C_4H_{11}N_2)ZnCl_3$ and $(C_4H_{11}N_2)ZnBr_3$ are isomorphic compounds of each other, crystallizing in *P*1 space group, and their unit cells have and only one asymmetric unit, containing one Zn, three Cl or Br atoms and one $(C_4H_{11}N_2)^+$ organic cation (Fig. 1). Whereas $(C_4H_{11}N_2)ZnI_3$ crystallizes in *Cc* space group, and its unit cell has four asymmetric unit, which is composed of a pair of $(C_4H_{11}N_2)ZnI_3$ molecule with different orientation (Fig. 1). Within their crystal structures, the six-membered $(C_4H_{11}N_2)^+$ ring shows a chair-shaped configuration with each C and N atom exhibiting sp^3 hybridization, suggesting that $(C_4H_{11}N_2)^+$ is non-π-conjugated. Each Zn^{2+} cation bonds with three halide anions and one N atom from organic cation, forming a tetrahedral $ZnNX_3$ groups (Fig. 1). The lengths of Zn–N are comparable with each other, with the values of 2.055(6) Å, 2.076(9) Å, and 2.074(11)–2.083(11) Å within $ZnNCl_3$, $ZnNBr_3$, and $ZnNI_3$ units. The size effect of halide anions induces the difference of Zn–X bonds, with the magnitude of Zn–I (2.568(2)–2.6067(19) Å) > Zn–Br (2.360(2)–2.4068(18) Å) > Zn–Cl (2.2291(19)–2.2735(19) Å). Obviously, Zn–N distances are smaller than those of Zn–X. Each $ZnNX_3$ tetrahedron is linked with $(C_4H_{11}N_2)^+$ organic cation *via* the brid-

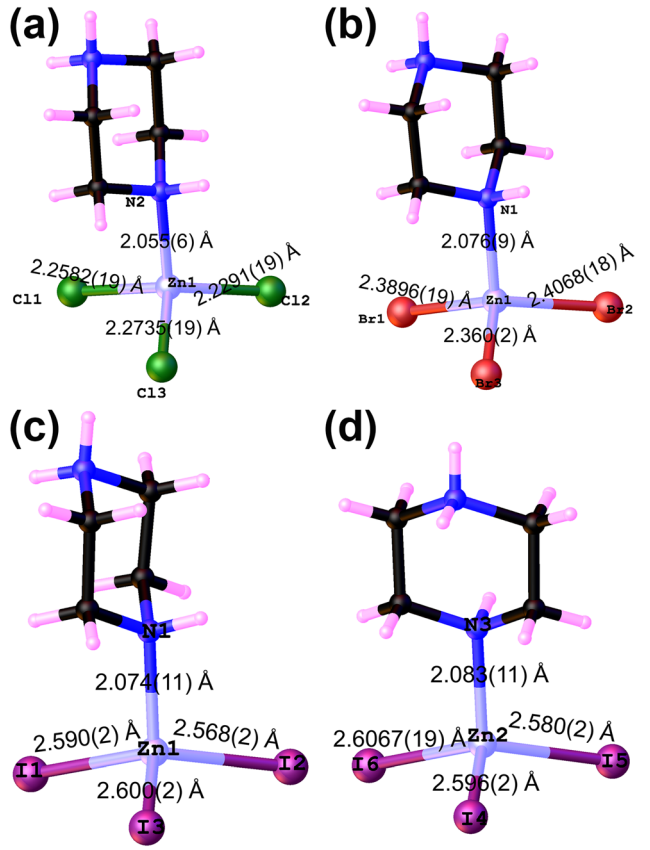

Fig. 1 The structures of 0D $(H_{11}C_4N_2)ZnX_3$ units, in which X = Cl (a), Br (b) and I (c–d).

ging of Zn–N coordination bond, forming a 0D $(C_4H_{11}N_2)ZnX_3$ neutral unit (Fig. 1).

The assembly mode of the 0D building block is consistent across the crystal structures of the three compounds (Fig. 2). In each compound, the 0D $(C_4H_{11}N_2)ZnX_3$ units are connected to each other through hydrogen bonds (Fig. 2a and b and Table S5†). Specifically, two halogen anions from one unit are linked to another pair of 0D $(C_4H_{11}N_2)ZnX_3$ units, while two H atoms from different N–H bonds bridge another pair of units. The distances of d(D–A) in the hydrogen bonds are 3.224(7)–3.282(7) Å, 3.398(12)–3.464(10) Å, and 3.645(15)–3.740(11) Å for N–H···Cl, N–H···Br, and N–H···I, respectively. Therefore, each 0D $(C_4H_{11}N_2)ZnX_3$ unit forms connections with four surrounding 0D units through four differently oriented hydrogen bonds (Fig. 2a and b). These interactions lead to the formation of two-dimensional $[(C_4H_{11}N_2)ZnX_3]_\infty$ infinite layers (Fig. 2a and b). Finally, the stacking of these 2D layers results in the overall 3D framework of $(C_4H_{11}N_2)ZnX_3$, in which the stacking form are –A–A–A– for Cl and Br compounds whereas –A–A′–A–A′– for $(C_4H_{11}N_2)ZnI_3$ (Fig. 2c and d).

Structure comparation

We delve into the structural disparities and their underlying causes between Cl, Br, and I compounds (Fig. 3a–c). Initially, the computations reveal that the distortion index of Δd_{tetr} for $ZnNCl_3$, $ZnNBr_3$, and $ZnNI_3$ are 0.034, 0.050, and 0.078, respectively, based on the formular of $\Delta d = 1/4\sum_{i=1}^{4}\left(\frac{d_{ij}-d_{av}}{d_{av}}\right)^2$. The distortion degree of $ZnNI_3$ significantly exceeds that of $ZnNCl_3$ and $ZnNBr_3$, aligning with the relative disparity in Zn–X and Zn–N bond lengths in their respective units. As the ionic radius gradually increases from Cl^- to I^-, it induces a progressive flexibility of the halide anion orbital. Consequently, with minimal alteration in the Zn–N radius, the elongation of Zn–X bond lengths gradually amplifies the tetrahedral distortion degree.

Subsequently, the $ZnNCl_3$ and $ZnNBr_3$ tetrahedra exhibit ideal alignment, with each tetrahedron's distortion direction being consistent, whereas neighboring $ZnNI_3$ not (Fig. 3). This results in the polarizability of $ZnNCl_3$ and $ZnNBr_3$ tetrahedra being able to align along a single polarization direction, while the polarizability of $ZnNI_3$ is partially counteracted. This phenomenon stems from the distinct space groups to which they belong (Fig. 3f and g). Cl and Br compounds crystallize in the *P*1 space group with the lowest symmetry and the fewest symmetry operations, with each unit cell containing only one $ZnNX_3$ tetrahedron, ensuring consistent orientations of adjacent $ZnNX_3$ groups. Conversely, $(C_4H_{11}N_2)ZnI_3$ crystallizes in the monoclinic *Cc* space group, leading to the orientations of adjacent $(C_4H_{11}N_2)ZnI_3$ molecules crossing each other, with the consistent components aligning along the polar axis. This observation is likely due to the size effect of the halide anions. The significantly larger ionic radius of I^- causes the volume of the $ZnNI_3$ tetrahedron to increase, rendering it unfeasible for the (*x*, *y*, *z*) symmetry operations in *P*1 space group to accommodate the $(H_{11}C_4N_2)ZnI_3$ molecules in space. Consequently, the latter can only be arranged in the *Cc* space group with more symmetry operations and energy-favorable.

Properties

TG-DTA analysis indicates that the initial decomposition temperatures of the Cl, Br, and I compounds are 300 °C, 334 °C, and 338 °C, respectively (Fig. S5†). These temperatures suggest substantial thermal stability, surpassing that of reported semi-organic NLO crystals or NLO organic–inorganic metal halides (OIMHs), such as $C(NH_2)_3SO_3F$ (162 °C),[72] $[C(NH_2)_3]_6(PO_4)_2{\cdot}3H_2O$ (100 °C), $(C_5H_6ON)(H_2PO_4)$ (166 °C),[73] and $(H_7C_3N_6)(H_6C_3N_6)HgCl_3$ (225 °C).[48] Additionally, these three crystals exhibit air stability, showing no signs of weathering or moisture absorption even after being stored in air at room temperature for several weeks (Fig. S2†).

The ultraviolet absorption spectrum shows that the transmittance of $(C_4H_{11}N_2)ZnCl_3$ at 190 nm is greater than 80% (Fig. 4a). And the wavelength-depended *F*(*R*) (absorption coefficient/scattering coefficient) values are nearly close to zero (Fig. 4a). These are consistent with most reported deep-UV crystals, such as $(NH_4)_2Na_3Li_9(SO_4)_7$,[36] $HfF_2(SO_4)$[40] and $Ba(NH_2SO_3)_2$,[45] indicating that $(C_4H_{11}N_2)ZnCl_3$ is able to transmit in the deep-UV region and possesses a wide bandgap larger than 6.20 eV. The absorption cutoff edges for $(C_4H_{11}N_2)$

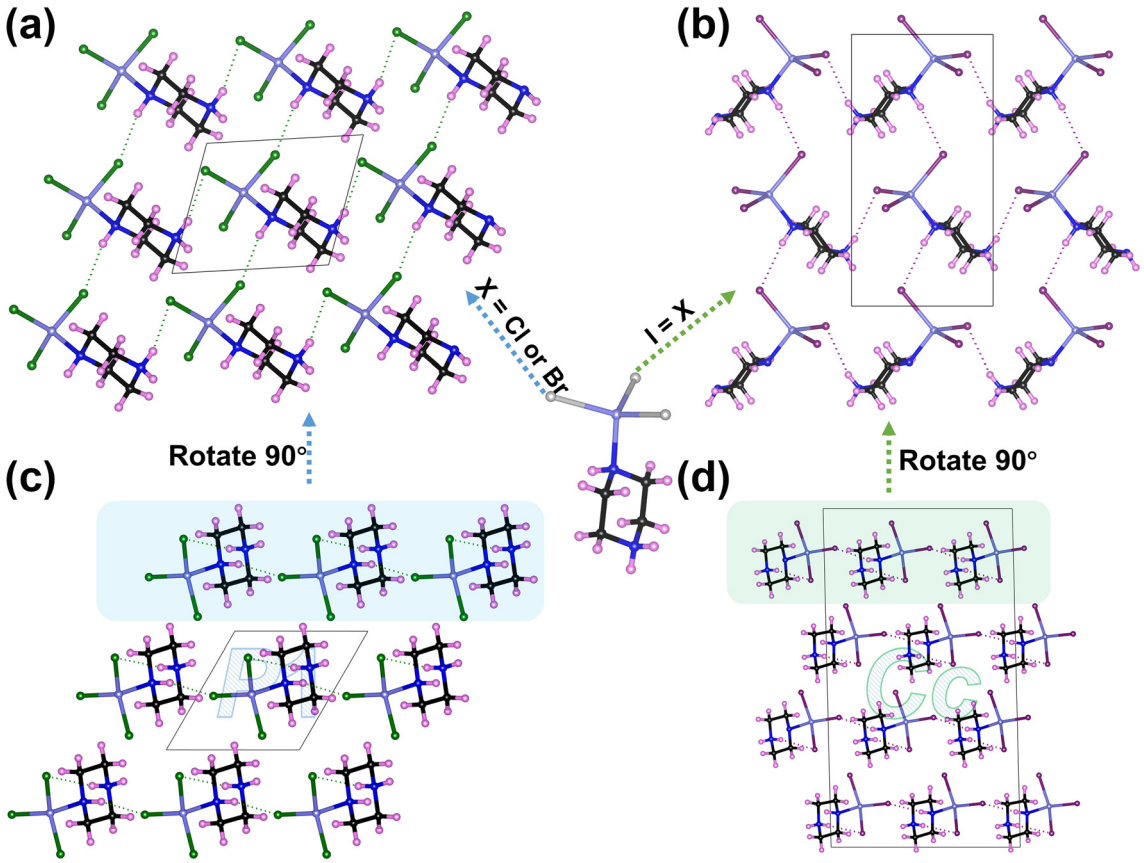

Fig. 2 Views of the structures of 2D $[(C_4H_{11}N_2)ZnCl_3]_\infty$ neutral layer along *a* direction (a), 3D $(C_4H_{11}N_2)ZnCl_3$ along *c* direction (b), 2D $[(C_4H_{11}N_2)ZnI_3]_\infty$ neutral layer along *a* direction, and 3D $(C_4H_{11}N_2)ZnI_3$ along *b* direction (d). The spheres of pink, violet-blue, blue, black, green, and dark purple respectively represent the atoms of H, Zn, N, C, Cl, and I.

$ZnBr_3$ and $(C_4H_{11}N_2)ZnI_3$ are 207 nm and 222 nm, respectively, corresponding to bandgaps of 5.53 eV and 4.52 eV (Fig. 4b and c). Notably, the halogen substitution from I to Cl increases the compound's bandgap and enhances its UV transmittance due to the difference in electronegativity of the halide anions. Importantly, the bandgaps of $(C_4H_{11}N_2)ZnCl_3$ and $(C_4H_{11}N_2)ZnBr_3$ are wider than all reported NLO-active OIMHs, including $(C_3N_6H_7)(C_3N_6H_6)HgCl_3$ (4.40 eV),[48] $(C_4H_{10}NO)_2Cd_2Cl_6$ (5.45 eV),[74] (L/D-$C_{10}H_{20}N_2O_4$)Cd_5Cl_{12} (5.42 eV),[75] $(C_{20}H_{20}P)CuBr_2$ (3.62 eV)[52] and L/D-$C_6H_{10}N_3O_2ZnBr_3$ (5.02 eV).[76] This highlights the exceptional deep-UV/UV transmittance and optical properties of $(C_4H_{11}N_2)ZnCl_3$ and $(C_4H_{11}N_2)ZnBr_3$. Their wide bandgaps also ensure good resistance to laser stability, with powder laser damage thresholds being 205.4 MW cm^{-2}, 150.2 MW cm^{-2}, and 87.0 MW cm^{-2} for Cl, Br, and I compounds, respectively, which are 51, 38 and 22 times that of $AgGaS_2$ (AGS: 4.0 MW cm^{-2}).

The SHG responses of $(C_4H_{11}N_2)ZnX_3$ were measured under 1064 nm laser radiation, and the results are presented in Fig. 4d. All compounds exhibit SHG activity, with efficiencies of 0.8, 2.5, and 2.1 times that of KH_2PO_4 (KDP) for $(C_4H_{11}N_2)ZnCl_3$, $(C_4H_{11}N_2)ZnBr_3$, and $(C_4H_{11}N_2)ZnI_3$, respectively, within the particle size range of 150–210 μm. Besides, Fig. 4e demonstrates that all compounds are phase-matchable. Combining the mentioned UV spectra, as shown in Fig. 6, we can draw some exciting conclusions. Firstly, $(C_4H_{11}N_2)ZnCl_3$ is the first reported deep-UV OIMHs with SHG activity (Fig. 5c), and its SHG response is comparable with those of known deep-UV compounds, including $(NH_4)_2Na_3Li_9(SO_4)_7$ (0.5 × KDP),[36] $Ba_3P_3O_{10}Cl$ (0.6 × KDP)[37] and $HfBa_3M_2F_{14}Cl$ (0.9 × KDP).[78] Secondly, the SHG effect of $(C_4H_{11}N_2)ZnBr_3$ surpasses that of currently reported OIMHs with a bandgap greater than 5.0 eV (Fig. 6a), including L/D-$C_{12}H_{20}N_6O_4Cd_2Cl_5$ (0.2 × KDP),[76] $(C_4H_{10}NO)_2Cd_2Cl_6$ (0.73 × KDP),[74] and (L/D-$C_{10}H_{20}N_2O_4$)Cd_5Cl_{12} (0.25 and 0.3 × KDP).[76] Additionally, the SHG effect of $(C_4H_{11}N_2)ZnBr_3$ is comparable to some recently reported semi-organic short UV NLO crystals, such as $(C_5H_6ON)(H_2PO_4)$ (3 × KDP),[77] $[C(NH_2)_3]_3PO_4{\cdot}2H_2O$ (1.5 × KDP)[73] and $Ba(SO_3NH_2)_2$ (2.7 × KDP).[46] Finally and most importantly, the substitution of I with Br in $(H_{11}C_4N_2)ZnI_3$ (2.1 × KDP, 4.52 eV) not only significantly increases the bandgap but also enhances its SHG effect. The anomalous relationship between bandgap and SHG effect due to halogen substitution is unprecedented, distinguishing it from previously reported OIMHs, such as $(C_6H_5(CH_2)_4NH_3)_4BiBr_7{\cdot}H_2O$ (0.4 × KDP, 3.52 eV) with $(C_6H_5(CH_2)_4NH_3)_4BiI_7{\cdot}H_2O$ (1.3 × AGS, 2.29 eV),[50] and

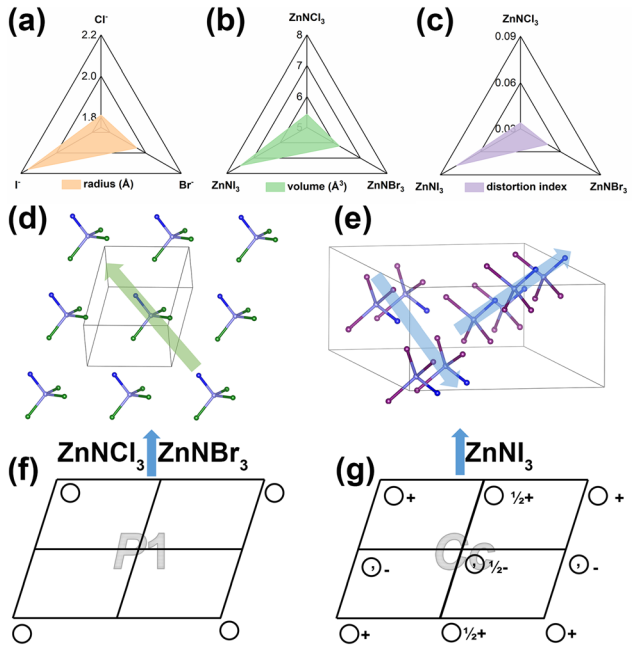

Fig. 3 The comparisons of radius of halide anions (a), as well as volume (b) and distortion index (c) of $ZnNX_3$ tetrahedra. The arrangement of $ZnNX_3$ tetrahedra in $(C_4H_{11}N_2)ZnCl(Br)_3$ (d) and $(C_4H_{11}N_2)ZnI_3$ (e). The green and blue arrow means the orientation of polarization. The symmetry of the space group of *P*1 (f) and *Cc* (g).

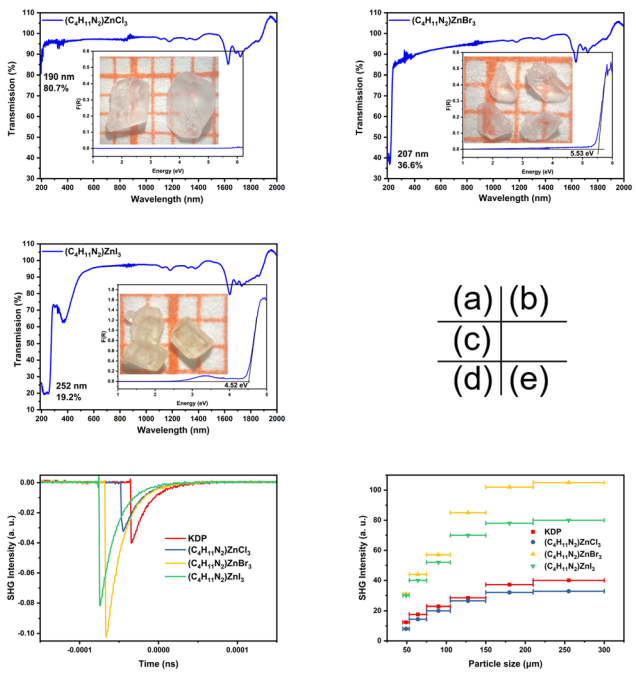

Fig. 4 UV transmittance spectra (a, b, c for Cl, Br, and I compounds, respectively). The inset shows the bandgaps and as-grown crystals. *F*(*R*) is the absorption coefficient/scattering coefficient. Oscilloscope traces of the SHG signals (150–210 μm) with 1064 nm laser radiation (d) and Phase-matching curves (e). KDP was used as references for the SHG measurements.

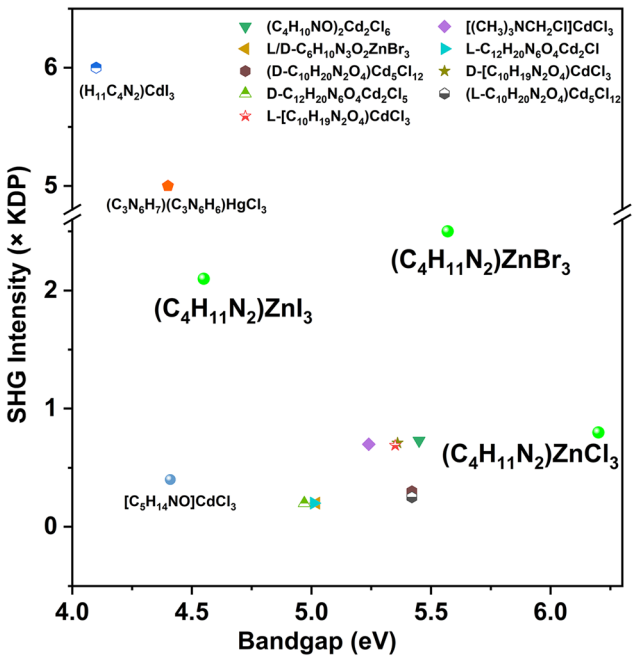

Fig. 5 SHG response and bandgap of selected NLO-active OIMHs with d^{10} cation.

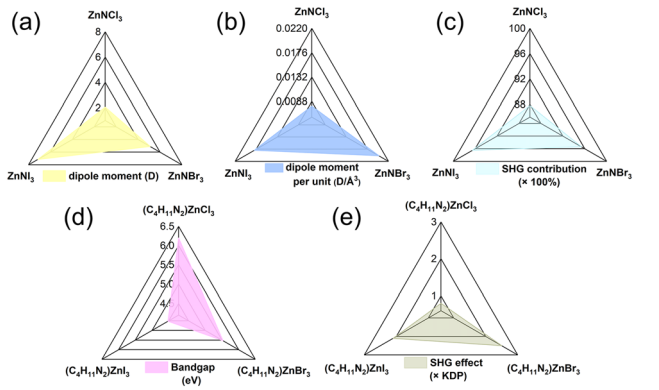

Fig. 6 The comparisons of dipole moment (a and b) and SHG contributions (c) of $ZnNX_3$ tetrahedra as well as bandgaps (d) and SHG effects (e) in $(C_4H_{11}N_2)ZnX_3$ (X = Cl, Br, I).

$Cs_3Pb_2(CH_3COO)_2Br_5$ (4 × KDP, 3.26 eV) with $Cs_3Pb_2(CH_3COO)_2I_5$ (8 × KDP, 2.55 eV).[55]

Structure–property relationship

We further analyzed the structure–property relationship of the three title compounds, especially the intrinsic reason why the Br compound can achieve SHG-bandgap balance optimization. Firstly, the size difference of halogens results in the volumes of $ZnNBr_3$ and $ZnNCl_3$ being much smaller than that of $ZnNI_3$, leading to different arrangement modes of this distorted tetrahedron in the structure (Fig. 3). Secondly, although the difference in halogen polarizability leads to a much larger distortion degree of $ZnNI_3$ than those of $ZnNBr_3$ and $ZnNCl_3$ (Fig. 3c),

the gap between $ZnNI_3$ and $ZnNBr_3$ narrows in terms of dipole moment (Fig. 6a). The dipole moments of $ZnNCl_3$, $ZnNBr_3$ and $ZnNI_3$ are 2.065, 5.113, and 6.692–7.306 D, respectively (Table S7†). Therefore, after further considering the arrangement of structural units and the unit cell volume, we found that the order of dipole moment per unit volume is $(C_4H_{11}N_2)ZnBr_3$ (0.020 DÅ^{-3}) > $(C_4H_{11}N_2)ZnI_3$ (0.018 D Å^{-3}) ≫ $(C_4H_{11}N_2)ZnCl_3$ (0.009 D Å^{-3}) (Fig. 6b). This order is consistent with the experimentally measured SHG effects, $(C_4H_{11}N_2)ZnCl_3$ (0.8 × KDP) ≪ $(C_4H_{11}N_2)ZnI_3$ (2.1 × KDP) < $(C_4H_{11}N_2)ZnBr_3$ (2.5 × KDP) (Fig. 6e). Therefore, considering that the SHG effect and bandgap are contradictory conditions for NLO crystals, we arrive at the following conclusions: ① chloride anion has the strongest electronegativity and the weakest polarizability. And, due to the perfectly aligned arrangement of $ZnNCl_3$ along the polarization direction in the structure, $(C_4H_{11}N_2)ZnCl_3$ can guarantee a moderate SHG effect (0.8 × KDP) while maintaining deep-UV transparency with wide bandgap (>6.2 eV); ② iodide anion has the weakest electronegativity and the strongest polarizability. Therefore, although the polarity of $ZnNI_3$ is partially cancelled out due to its non-ideal arrangement, its smaller bandgap ensures a strong SHG effect (2.1 × KDP; 4.52 eV); ③ the slightly larger radius of bromide anion compared to chloride allows $ZnNBr_3$ to adopt the same arrangement mode as $ZnNCl_3$, with perfectly superimposed polarity. Therefore, compared with $(C_4H_{11}N_2)ZnCl_3$, the SHG effect of $(C_4H_{11}N_2)ZnBr_3$ is dramatically enhanced at the expense of a partial bandgap sacrifice (Fig. 6d and e). More importantly, compared with $(C_4H_{11}N_2)ZnI_3$, $(C_4H_{11}N_2)ZnBr_3$ exhibits an enhanced SHG effect while significantly widening the band gap, thus achieving optimization of the SHG-bandgap balance (Fig. 6d and e).

Systematic theoretical calculations were conducted to analyze the band structures and densities of states (DOS) of the title compounds. The calculated band structures for these compounds are illustrated in Fig. S6.† The theoretical bandgaps (4.815 eV, 4.404 eV, and 4.304 eV for Cl, Br, and I compounds, respectively) roughly align with experimental values. For $(C_4H_{11}N_2)ZnCl_3$ and $(C_4H_{11}N_2)ZnBr_3$, the theoretical bandgaps deviate significantly from experimental values due to the discontinuity of the exchange–correlation function. As shown in Fig. 7a–c, The Cl-3p, Br-4p, and I-5p states predominantly contribute to the top of the valence band (VB), while the Zn-4s state is the primary contributor to the bottom of the conduction band (CB). Additionally, with the substitution of Cl by Br and I, the contribution of X-ns^{2}np^6 orbitals to the

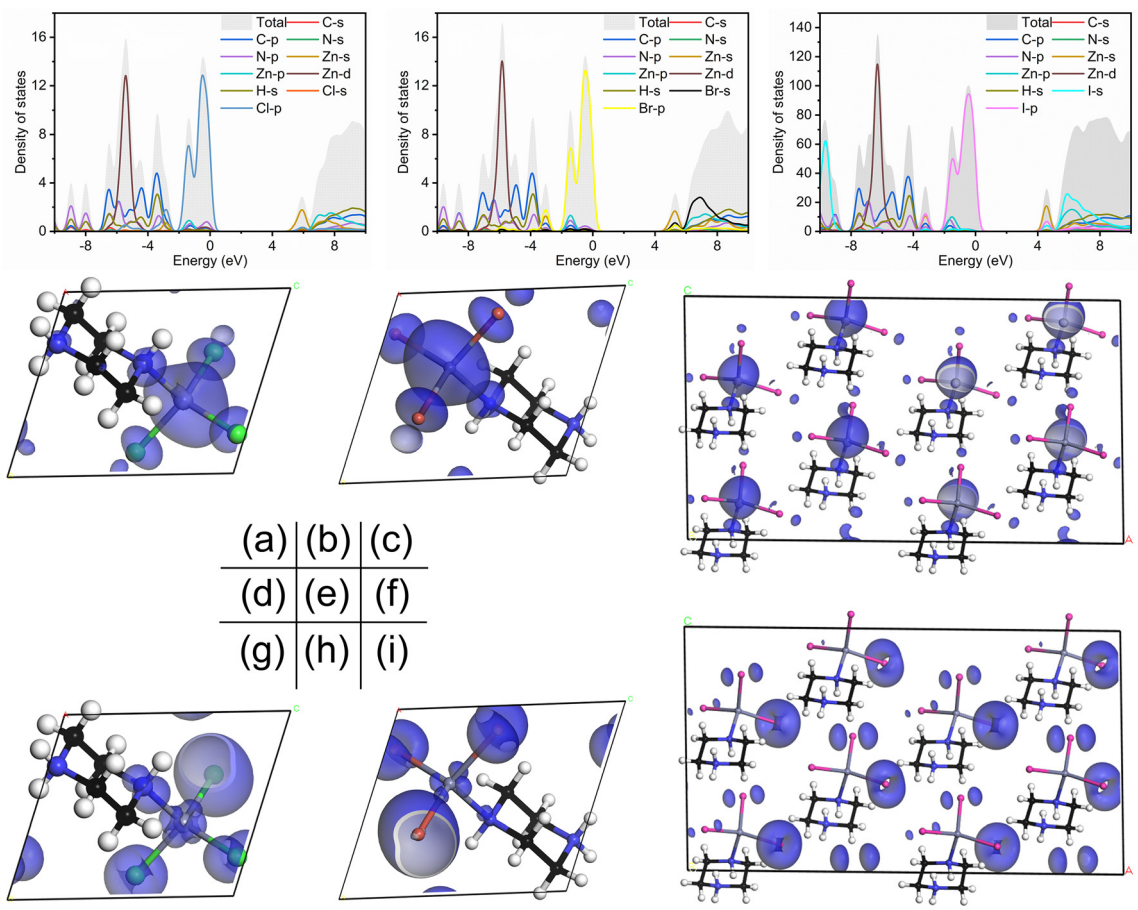

Fig. 7 The DOS (a–c) as well as the SHG density distribution in VB (d–f) and CB (g–i) for $(C_4H_{11}N_2)ZnX_3$ (X = Cl, Br, I).

bottom of the CB becomes significant and shows an increasing trend.

We further calculated the optical properties (birefringence and second-order nonlinear optical coefficients) of the title compounds. A principal axis transformation was first conducted; for the triclinic systems of $(C_4H_{11}N_2)ZnCl_3$ and $(C_4H_{11}N_2)ZnBr_3$, the rotation angles between the crystallographic axes and the principal dielectric axes are shown in Table S8.† For the monoclinic system of $(C_4H_{11}N_2)ZnI_3$, the rotation angle between the crystallographic axes and the principal dielectric axes is 25.173°. As depicted in Fig. S7,† the birefringence values for the Cl, Br, and I compounds are 0.04@546 nm, 0.06@546 nm, and 0.08@546 nm, relating to the shortest type-I phase-matchable wavelength of 371 nm, 335 nm, and 451 nm, respectively. It is worth noting that from $(C_4H_{11}N_2)ZnI_3$ to $(C_4H_{11}N_2)ZnBr_3$, halide substitution has achieved a triple increase in SHG effect, bandgap, and phase-matching capability. We also calculated the effective second-order nonlinear optical coefficients (d_{eff}), which are 0.522 pm V^{-1}, 0.847 pm V^{-1}, and 1.344 pm V^{-1} for Cl, Br, and I compounds, respectively. Notably, the d_{eff} of the $(C_4H_{11}N_2)ZnBr_3$ is 2.2 times that of KDP (0.39 pm V^{-1}), aligning closely with the experimental value (2.5 × KDP).

The origins of the SHG effects for the three title compounds were elucidated through computational analysis of the SHG density distribution (Fig. 6d–i). In the VB, the Cl-3p, Br-4p, and I-5p orbitals predominantly contribute to the SHG effect in their respective compounds. For the Cl and Br analogs, the Zn-3d and N-2p orbitals associated with the Zn-N bonds also play a significant role in the SHG effect, but a contribution that is negligible in the I analog. Furthermore, within the CB, the Zn-3s orbital is identified as the primary contributor to the SHG, with additional contributions from the Cl-3p/Br-4p/I-5p and N-2p orbitals on the Zn–N bonds. The quantitative contributions from the piperazine cation and the distorted tetrahedral $ZnNX_3$ anion to the SHG were assessed, with the $ZnNCl_3$, $ZnNBr_3$, and $ZnNI_3$ units exhibiting SHG contribution percentages of 87.8%, 95.4%, and 96.5%, respectively (Fig. 6e). This trend indicates a progressive increase in SHG contribution as the halogen substitution proceeds from chlorine to bromine to iodine, correlating with a decrease in electronegativity and an increase in polarizability of the halogen anions. Concurrently, the impact of the Zn–X bonds on the SHG effect of the compounds becomes more pronounced.

Conclusions

This study culminates in the discovery of three novel noncentrosymmetric piperazine zinc halide compounds, $(C_4H_{11}N_2)ZnX_3$ (X = Cl, Br, I), achieved through strategic halide substitution. Notably, $(C_4H_{11}N_2)ZnCl_3$ stands as the pioneering deep-UV nonlinear optical OIMH with a SHG effect of 0.8 × KDP. Our findings underscore the exceptional case of $(C_4H_{11}N_2)ZnBr_3$, which achieves a remarkable bandgap expansion to 5.53 eV without compromising on a potent SHG response (2.5 × KDP), setting a new benchmark among OIMHs with bandgaps greater than 5.0 eV. The progression from chlorine to bromine and iodine in halide substitution is shown to progressively enhance SHG contributions, correlating with reduced electronegativity and heightened polarizability of the halide ions. These findings not only broaden the scope of OIMHs with tailored optical properties but also highlight $(C_4H_{11}N_2)ZnBr_3$ as a prime candidate for short-wavelength UV NLO crystal applications. The work underscores the importance of halide choice in engineering OIMHs with optimized SHG-bandgap balance and sets the stage for further explorations into high-performance NLO materials.

Author contributions

Chen Jin and Wu Huai-Yu: conceptualization, methodology, writing – original draft, data curation, visualization; Xu Miao-Bin, Wang Ming-Chang, Chen Qian-Qian and Bing-Xuan Li: data curation; Hu Chun-Li: formal analysis; Hu Chun-Li, Du Ke-Zhao and Chen Jin: writing – review & editing, supervision.

Data availability

Crystallographic data for $(H_{11}C_4N_2)ZnX_3$ (X = Cl, Br, I) have been deposited with the CCDC under deposition numbers 2313121–2313123† and can be obtained from **https://www.ccdc.cam.ac.uk/**. Other data are available from the authors upon request.

Conflicts of interest

There are no conflicts to declare.

Acknowledgements

Our work has been supported by the National Natural Science Foundation of China (No. 22205037 and 22373014) and Natural Science Foundation of Fujian Province (2023J01498).

References

1 C. Chen, Y. Wang, B. Wu, K. Wu, W. Zeng and L. Yu, Design and synthesis of an ultraviolet-transparent nonlinear optical crystal $Sr_2Be_2B_2O_7$, *Nature*, 1995, **373**, 322–324.

2 M. Mutailipu, J. Han, Z. Li, F. Li, J. Li, F. Zhang, X. Long, Z. Yang and S. Pan, Achieving the full-wavelength phase-matching for efficient nonlinear optical frequency conversion in $C(NH_2)_3BF_4$, *Nat. Photonics*, 2023, **17**, 694–701.

3 X. Liu, Y.-C. Yang, M.-Y. Li, L. Chen and L.-M. Wu, Anisotropic structure building unit involving diverse chemical bonds: a new opportunity for high-performance

second-order NLO materials, *Chem. Soc. Rev.*, 2023, **52**, 8699–8720.
4 M. Mutailipu, K. R. Poeppelmeier and S.-L. Pan, Borates: A Rich Source for Optical Materials, *Chem. Rev.*, 2021, **121**, 1130–1202.
5 J. Chen, C.-L. Hu, F. Kong and J.-G. Mao, High-Performance Second-Harmonic-Generation (SHG) Materials: New Developments and New Strategies, *Acc. Chem. Res.*, 2021, **54**, 2775–2783.
6 J. Xu, X. Li, J. Xiong, C. Yuan, S. Semin, T. Rasing and X.-H. Bu, Halide Perovskites for Nonlinear Optics, *Adv. Mater.*, 2020, **32**, 1806736.
7 Y. Kang, C. Yang, J. Gou, Y. Zhu, Q. Zhu, W. Xu and Q. Wu, From $Cd(SCN)_2(CH_4N_2S)_2$ to $Cd(SCN)_2(C_4H_6N_2)_2$: Controlling Sulfur Content in Thiocyanate Systems Significantly Improves the Overall Performance of UV Nonlinear Optical Materials, *Angew. Chem., Int. Ed.*, 2024, **63**, e202402086.
8 X. Zhang, L. Kang, P. Gong, Z. Lin and Y. Wu, Nonlinear Optical Oxythiophosphate Approaching the Good Balance with Wide Ultraviolet Transparency, Strong Second Harmonic Effect, and Large Birefringence, *Angew. Chem., Int. Ed.*, 2021, **60**, 6386–6390.
9 H. Fan, N. Ye and M. Luo, New Functional Groups Design toward High Performance Ultraviolet Nonlinear Optical Materials, *Acc. Chem. Res.*, 2023, **56**, 3099–3109.
10 Y. Li, J. Luo and S. Zhao, Local Polarity-Induced Assembly of Second-Order Nonlinear Optical Materials, *Acc. Chem. Res.*, 2022, **55**, 3460–3469.
11 M. Mutailipu, Z. Yang and S. Pan, Toward the Enhancement of Critical Performance for Deep-Ultraviolet Frequency-Doubling Crystals Utilizing Covalent Tetrahedra, *Acc. Mater. Res.*, 2021, **2**, 282–291.
12 L. Kang, F. Liang, X. Jiang, Z. Lin and C. Chen, First-Principles Design and Simulations Promote the Development of Nonlinear Optical Crystals, *Acc. Chem. Res.*, 2020, **53**, 209–217.
13 M. Mutailipu, M. Zhang, Z. Yang and S. Pan, Targeting the Next Generation of Deep-Ultraviolet Nonlinear Optical Materials: Expanding from Borates to Borate Fluorides to Fluorooxoborates, *Acc. Chem. Res.*, 2019, **52**, 791–801.
14 Z. Xia and K. R. Poeppelmeier, Chemistry-Inspired Adaptable Framework Structures, *Acc. Chem. Res.*, 2017, **50**, 1222–1230.
15 K. M. Ok, Toward the Rational Design of Novel Noncentrosymmetric Materials: Factors Influencing the Framework Structures, *Acc. Chem. Res.*, 2016, **49**, 2774–2785.
16 B. Zhang and Z. Chen, Recent advances of inorganic phosphates with UV/DUV cutoff edge and large second harmonic response, *Chin. J. Struct. Chem.*, 2023, **42**, 100033.
17 Z. Bai, J. Lee, C.-L. Hu, G. Zou and K. M. Ok, Hydrogen bonding bolstered head-to-tail ligation of functional chromophores in a 0D SbF_3·glycine adduct for a short-wave ultraviolet nonlinear optical material, *Chem. Sci.*, 2024, **15**, 6572–6576.
18 Y.-N. Zhang, Q.-F. Li, B.-B. Chen, Y.-Z. Lan, J.-W. Cheng and G.-Y. Yang, $Na_3B_6O_{10}(HCOO)$: an ultraviolet nonlinear optical sodium borate-formate, *Inorg. Chem. Front.*, 2022, **9**, 5032–5038.
19 W.-F. Chen, J.-Y. Lu, J.-J. Li, Y.-Z. Lan, J.-W. Cheng and G.-Y. Yang, $Sr_2[B_5O_8(OH)]_2$·$[B(OH)_3]$·H_2O: A Strontium Borate That Shows Deep-Ultraviolet-Transparent Nonlinear Optical Properties, *Chem. – Eur. J.*, 2024, **30**, e202400739.
20 H. Su, Z. Yan, X. Hou and M. Zhang, Fluorooxoborates: A precious treasure of deep-ultraviolet nonlinear optical materials, *Chin. J. Struct. Chem.*, 2023, **42**, 100027.
21 D. Gao, H. Wu, Z. Hu, J. Wang, Y. Wu and H. Yu, Recent advances in F-containing iodate nonlinear optical materials, *Chin. J. Struct. Chem.*, 2023, **42**, 100014.
22 Q. Shi, L. Dong and Y. Wang, Evaluating refractive index and birefringence of nonlinear optical crystals: Classical methods and new developments, *Chin. J. Struct. Chem.*, 2023, **42**, 100017.
23 J.-H. Wu, B. Zhang, T.-K. Jiang, F. Kong and J.-G. Mao, From $Cs_8Sb_4Nb_5O_5F_{35}$ to $Cs_6Sb_4Mo_3O_5F_{26}$: The first non-centrosymmetric fluoroantimonite with d^{10} transition metal, *Chin. J. Struct. Chem.*, 2023, **42**, 100016.
24 J.-H. Wu, C.-L. Hu, T.-K. Jiang, J.-G. Mao and F. Kong, Highly Birefringent d0 Transition Metal Fluoroantimonite in the Mid Infrared Band: Order–Disorder Regulation by Cationic Size, *J. Am. Chem. Soc.*, 2023, **145**, 24416–24424.
25 J. Chen, C.-L. Hu, F.-F. Mao, J.-H. Feng and J.-G. Mao, A Facile Route to Nonlinear Optical Materials: Three-Site Aliovalent Substitution Involving One Cation and Two Anions, *Angew. Chem., Int. Ed.*, 2019, **58**, 2098–2102.
26 M. Mutailipu, F. Li, C. Jin, Z. Yang, K. R. Poeppelmeier and S. Pan, Strong Nonlinearity Induced by Coaxial Alignment of Polar Chain and Dense $[BO_3]$ Units in $CaZn_2(BO_3)_2$, *Angew. Chem., Int. Ed.*, 2022, **61**, e202202096.
27 H. Qiu, F. Li, Z. Li, Z. Yang, S. Pan and M. Mutailipu, Breaking the Inherent Interarrangement of $[B_3O_6]$ Clusters for Nonlinear Optics with Orbital Hybridization Enhancement, *J. Am. Chem. Soc.*, 2023, **145**, 24401–24407.
28 H. Qiu, F. Li, C. Jin, Z. Yang, J. Li, S. Pan and M. Mutailipu, Fluorination Strategy Towards Symmetry Breaking of Boron-centered Tetrahedron for Poly-fluorinated Optical Crystals, *Angew. Chem., Int. Ed.*, 2023, **63**, e202316194.
29 F. Ding, K. J. Griffith, W. Zhang, S. Cui, C. Zhang, Y. Wang, K. Kamp, H. Yu, P. S. Halasyamani, Z. Yang, S. Pan and K. R. Poeppelmeier, $NaRb_6(B_4O_5(OH)_4)_3(BO_2)$ Featuring Noncentrosymmetry, Chirality, and the Linear Anionic Group BO_2^-, *J. Am. Chem. Soc.*, 2023, **145**, 4928–4933.
30 H. Pei, X. Wang, J. Zhang, F. Zhang, Z. Yang and S. Pan, $Ba_2B_9O_{13}F_4$·BF_4: first fluorooxoborate with unprecedented infinite $[B_{18}O_{26}F_8]$ tubes and deep-ultraviolet cutoff edge, *Sci. China: Chem.*, 2023, **66**, 1073–1077.
31 H. Liu, H. Wu, Z. Hu, J. Wang, Y. Wu and H. Yu, $Cs_3[(BOP)_2(B_3O_7)_3]$: A Deep-Ultraviolet Nonlinear Optical Crystal Designed by Optimizing Matching of Cation and Anion Groups, *J. Am. Chem. Soc.*, 2023, **145**, 12691–12700.

32 Y. Shang, J. Xu, H. Sha, Z. Wang, C. He, R. Su, X. Yang and X. Long, Nonlinear optical inorganic sulfates: The improvement of the phase matching ability driven by the structural modulation, *Coord. Chem. Rev.*, 2023, **494**, 215345.
33 X. Chen, Y. Li, J. Luo and S. Zhao, Recent advances in non-π-conjugated nonlinear optical sulfates with deep-UV absorption edge, *Chin. J. Struct. Chem.*, 2023, **42**, 100044.
34 M. Mutailipu and S. Pan, Emergent Deep-Ultraviolet Nonlinear Optical Candidates, *Angew. Chem., Int. Ed.*, 2019, **59**, 20302–20317.
35 J. Dang, D. Mei, Y. Wu and Z. Lin, A comprehensive survey on nonlinear optical phosphates: Role of multicoordinate groups, *Coord. Chem. Rev.*, 2021, **431**, 213692.
36 Y. Li, F. Liang, S. Zhao, L. Li, Z. Wu, Q. Ding, S. Liu, Z. Lin, M. Hong and J. Luo, Two Non-π-Conjugated Deep-UV Nonlinear Optical Sulfates, *J. Am. Chem. Soc.*, 2019, **141**, 3833–3837.
37 P. Yu, L.-M. Wu, L.-J. Zhou and L. Chen, Deep-Ultraviolet Nonlinear Optical Crystals: $Ba_3P_3O_{10}X$ (X = Cl, Br), *J. Am. Chem. Soc.*, 2014, **136**, 480–487.
38 S. Zhao, X. Yang, Y. Yang, X. Kuang, F. Lu, P. Shan, Z. Sun, Z. Lin, M. Hong and J. Luo, Non-Centrosymmetric $RbNaMgP_2O_7$ with Unprecedented Thermo-Induced Enhancement of Second Harmonic Generation, *J. Am. Chem. Soc.*, 2018, **140**, 1592–1595.
39 Y. Li, C. Yin, X. Yang, X. Kuang, J. Chen, L. He, Q. Ding, S. Zhao, M. Hong and J. Luo, A Nonlinear Optical Switchable Sulfate of Ultrawide Bandgap, *CCS Chem.*, 2020, **3**, 2298–2306.
40 C. Wu, C. Jiang, G. Wei, X. Jiang, Z. Wang, Z. Lin, Z. Huang, M. G. Humphrey and C. Zhang, Toward Large Second-Harmonic Generation and Deep-UV Transparency in Strongly Electropositive Transition Metal Sulfates, *J. Am. Chem. Soc.*, 2023, **145**, 3040–3046.
41 J. Lu, J.-N. Yue, L. Xiong, W.-K. Zhang, L. Chen and L.-M. Wu, Uniform Alignment of Non-π-Conjugated Species Enhances Deep Ultraviolet Optical Nonlinearity, *J. Am. Chem. Soc.*, 2019, **141**, 8093–8097.
42 X. Wang, X. Leng, Y. Kuk, J. Lee, Q. Jing and K. M. Ok, Deep-Ultraviolet Transparent Mixed Metal Sulfamates with Enhanced Nonlinear Optical Properties and Birefringence, *Angew. Chem., Int. Ed.*, 2023, **63**, e202315434.
43 Z. Bai and K. M. Ok, Designing Sulfate Crystals with Strong Optical Anisotropy through π-Conjugated Tailoring, *Angew. Chem., Int. Ed.*, 2023, **63**, e202315311.
44 H. Tian, N. Ye and M. Luo, Sulfamide: A Promising Deep-Ultraviolet Nonlinear Optical Crystal Assembled from Polar Covalent $[SO_2(NH_2)_2]$ Tetrahedra, *Angew. Chem., Int. Ed.*, 2022, **61**, e202200395.
45 H. Tian, C. Lin, X. Zhao, F. Xu, C. Wang, N. Ye and M. Luo, $Ba(SO_3CH_3)_2$: a Deep-Ultraviolet Transparent Crystal with Excellent Optical Nonlinearity Based on a New Polar Non-π-conjugated NLO Building Unit $SO_3CH_3^-$, *CCS Chem.*, 2022, **5**, 2497–2505.
46 X. Hao, M. Luo, C. Lin, G. Peng, F. Xu and N. Ye, M $(NH_2SO_3)_2$ (M=Sr, Ba): Two Deep-Ultraviolet Transparent Sulfamates Exhibiting Strong Second Harmonic Generation Responses and Moderate Birefringence, *Angew. Chem., Int. Ed.*, 2021, **60**, 7621–7625.
47 H.-Y. Wu, C.-L. Hu, M.-B. Xu, Q.-Q. Chen, N. Ma, X.-Y. Huang, K.-Z. Du and J. Chen, From $H_{12}C_4N_2CdI_4$ to $H_{11}C_4N_2CdI_3$: a highly polarizable $CdNI_3$ tetrahedron induced a sharp enhancement of second harmonic generation response and birefringence, *Chem. Sci.*, 2023, **14**, 9533–9542.
48 Z. Bai, J. Lee, H. Kim, C.-L. Hu and K. M. Ok, Unveiling the Superior Optical Properties of Novel Melamine-Based Nonlinear Optical Material with Strong Second-Harmonic Generation and Giant Optical Anisotropy, *Small*, 2023, **19**, 2301756.
49 L. Liu, Z. Bai, L. Hu, D. Wei, Z. Lin and L. Zhang, A melamine-based organic–inorganic hybrid material revealing excellent optical performance and moderate thermal stability, *J. Mater. Chem. C*, 2021, **9**, 7452–7457.
50 D. Chen, S. Hao, L. Fan, Y. Guo, J. Yao, C. Wolverton, M. G. Kanatzidis, J. Zhao and Q. Liu, Broad Photoluminescence and Second-Harmonic Generation in the Noncentrosymmetric Organic–Inorganic Hybrid Halide $(C_6H_5(CH_2)_4NH_3)_4MX_7{\cdot}H_2O$ (M = Bi, In, X = Br or I), *Chem. Mater.*, 2021, **33**, 8106–8111.
51 Y. Kang and Q. Wu, A review of the relationship between the structure and nonlinear optical properties of organic-inorganic hybrid materials, *Coord. Chem. Rev.*, 2024, **498**, 215458.
52 J. Wu, Y. Guo, J.-L. Qi, W.-D. Yao, S.-X. Yu, W. Liu and S.-P. Guo, Multi-Stimuli Responsive Luminescence and Domino Phase Transition of Hybrid Copper Halides with Nonlinear Optical Switching Behavior, *Angew. Chem., Int. Ed.*, 2023, **62**, e202301937.
53 X.-Y. Li, Q. Wei, C.-L. Hu, J. Pan, B.-X. Li, Z.-Z. Xue, X.-Y. Li, J.-H. Li, J.-G. Mao and G.-M. Wang, Achieving Large Second Harmonic Generation Effects via Optimal Planar Alignment of Triangular Units, *Adv. Funct. Mater.*, 2023, **33**, 2210718.
54 Y. Liu, Y.-P. Gong, S. Geng, M.-L. Feng, D. Manidaki, Z. Deng, C. C. Stoumpos, P. Canepa, Z. Xiao, W.-X. Zhang and L. Mao, Hybrid Germanium Bromide Perovskites with Tunable Second Harmonic Generation, *Angew. Chem., Int. Ed.*, 2022, **61**, e202208875.
55 Q.-R. Shui, H.-X. Tang, R.-B. Fu, Y.-B. Fang, Z.-J. Ma and X.-T. Wu, $Cs_3Pb_2(CH_3COO)_2X_5$ (X=I, Br): Halides with Strong Second-Harmonic Generation Response Induced by Acetate Groups, *Angew. Chem., Int. Ed.*, 2021, **60**, 2116–2119.
56 P. Qian, Y. Li, J. Cheng, J. Li, H. Zeng, L. Huang, G. Zou and Z. Lin, Multiple Functions of l-Thioproline in the Synthesis of Chiral Metal Bromides Showing Second-Harmonic-Generation Responses, *Inorg. Chem.*, 2024, **63**, 8013–8017.
57 S.-F. Yan, Y. Guo, W. Liu, S.-P. Guo and J. Wu, Tellurium(IV) Halide Achieving Effective Nonlinear-Optical Activity: The Role of Chiral Ligands and Lattice Distortion, *Inorg. Chem.*, 2024, **63**, 73–77.

58 J.-L. Qi, J. Wu, Y. Guo, Z.-P. Xu, W. Liu and S.-P. Guo, Quasi-linear CuX_2 (X = Cl, Br) motif-built hybrid copper halides realizing encouraging nonlinear optical activities, *Inorg. Chem. Front.*, 2023, **10**, 3319–3325.

59 W. He, Y. Yang, C. Li, W. P. D. Wong, F. Cimpoesu, A. M. Toader, Z. Wu, X. Wu, Z. Lin, Q.-h. Xu, K. Leng, A. Stroppa and K. P. Loh, Near-90° Switch in the Polar Axis of Dion–Jacobson Perovskites by Halide Substitution, *J. Am. Chem. Soc.*, 2023, **145**, 14044–14051.

60 R. H. Blessing, An empirical correction for absorption anisotropy, *Acta Crystallogr., Sect. A: Found. Crystallogr.*, 1995, **51**, 33–38.

61 G. M. Sheldrick, Crystal structure refinement with it SHELXL, *Acta Crystallogr.*, 2015, **71**, 3–8.

62 A. L. Spek, Single-crystal structure validation with the program it PLATON, *J. Appl. Crystallogr.*, 2003, **36**, 7–13.

63 P. K. a. F. Munk, An Article on Optics of Paint Layers, *Z. Tech. Phys.*, 1931, 259–274.

64 S. K. Kurtz and T. T. Perry, A Powder Technique for the Evaluation of Nonlinear Optical Materials, *J. Appl. Phys.*, 2003, **39**, 3798–3813.

65 M. D. Segall, J. D. L. Philip, M. J. Probert, C. J. Pickard, P. J. Hasnip, S. J. Clark and M. C. Payne, First-principles simulation: ideas, illustrations and the CASTEP, *J. Phys.: Condens. Matter*, 2002, **14**, 2717.

66 V. Milman, B. Winkler, J. A. White, C. J. Pickard, M. C. Payne, E. V. Akhmatskaya and R. H. Nobes, Electronic structure, properties, and phase stability of inorganic crystals: A pseudopotential plane-wave study, *J. Quantum Chem.*, 2000, **77**, 895–910.

67 J. P. Perdew, K. Burke and M. Ernzerhof, Generalized Gradient Approximation Made Simple, *Phys. Rev. Lett.*, 1996, **77**, 3865–3868.

68 J. S. Lin, A. Qteish, M. C. Payne and V. Heine, Optimized and transferable nonlocal separable *ab initio* pseudopotentials, *Phys. Rev. B: Condens. Matter Mater. Phys.*, 1993, **47**, 4174.

69 J. Lin, M.-H. Lee, Z.-P. Liu, C. Chen and C. J. Pickard, Mechanism for linear and nonlinear optical effects in β–BaB_2O_4 crystals, *Phys. Rev. B: Condens. Matter Mater. Phys.*, 1999, **60**, 13380.

70 S. N. Rashkeev, W. R. Lambrecht and B. Segall, Efficient *ab initio* method for the calculation of frequency-dependent second-order optical response in semiconductors, *Phys. Rev. B: Condens. Matter Mater. Phys.*, 1998, **57**, 3905.

71 Y.-P. Lin, S. Hu, J. Xu, Z. Zhang, X. Qi, X. Lu, J. Jin, X.-Y. Huang, Q. Xu, Z. Deng, Z. Xiao and K.-Z. Du, Bright green emitter of Mn-doped $C_4H_{12}N_2ZnX_4$ (X = Cl, Br) for X-ray radiography and WLEDs, *Chem. Eng. J.*, 2023, **468**, 143818.

72 M. Luo, C. Lin, D. Lin and N. Ye, Rational Design of the Metal-Free $KBe_2BO_3F_2$ (KBBF) Family Member $C(NH_2)_3SO_3F$ with Ultraviolet Optical Nonlinearity, *Angew. Chem., Int. Ed.*, 2020, **59**, 15978–15981.

73 X. Wen, C. Lin, M. Luo, H. Fan, K. Chen and N. Ye, $[C(NH_2)_3]_3PO_4{\cdot}2H_2O$: A new metal-free ultraviolet nonlinear optical phosphate with large birefringence and second-harmonic generation response, *Sci. China Mater.*, 2021, **64**, 2008–2016.

74 D. Sun, D. Wang, Y. Dang, S. Zhang, H. Chen, R. Hou, K. Wu and C. Shen, Organic–Inorganic Hybrid Noncentrosymmetric $(Morpholinium)_2Cd_2Cl_6$ Single Crystals: Synthesis, Nonlinear Optical Properties, and Stability, *Inorg. Chem.*, 2022, **61**, 8076–8082.

75 J. Cheng, Y. Deng, X. Dong, J. Li, L. Huang, H. Zeng, G. Zou and Z. Lin, Homochiral Hybrid Organic–Inorganic Cadmium Chlorides Directed by Enantiopure Amino Acids, *Inorg. Chem.*, 2022, **61**, 11032–11035.

76 W. Seo and K. M. Ok, Novel noncentrosymmetric polar coordination compounds derived from chiral histidine ligands, *Inorg. Chem. Front.*, 2021, **8**, 4536–4543.

77 J. Lu, X. Liu, M. Zhao, X.-B. Deng, K.-X. Shi, Q.-R. Wu, L. Chen and L.-M. Wu, Discovery of NLO Semiorganic $(C_5H_6ON)^+(H_2PO_4)^-$: Dipole Moment Modulation and Superior Synergy in Solar-Blind UV Region, *J. Am. Chem. Soc.*, 2021, **143**, 3647–3654.

78 Y. Mei, C.-L. Hu, R.-L. Tang, W.-D. Yao, W. Liu and S.-P. Guo, $KBa_3M_2F_{14}Cl$ (M = Zr, Hf): novel short-wavelength mixed metal halides with the largest second-harmonic generation responses contributed by mixed functional moieties, *Chem. Sci.*, 2024, **15**, 8500–8505.